Word count: 5053

The electrical conductivity of albite feldspar: implications for oceanic lower crustal sequences and subduction zones

Running Title: EC Measurements of andesine at Crustal PT Conditions

Version: Revision 1 (Accept with revisions) Corrected version

Date: 10/03/2021

Journal: *American Mineralogist*

George M. Amulele[1,2†], Anthony W. Lanati[1,3*†], and Simon M. Clark[1]

[1] Australian Research Council Centre of Excellence for Core to Crust Fluid Systems (CCFS), Department of Earth and Environmental Sciences, Macquarie University, Balaclava Road, North Ryde, NSW 2109, Sydney, Australia.

[2] Earth, Environmental and Planetary Sciences, Case Western Reserve University, 10900 Euclid Avenue, OH 44106, U. S. A

[3] Institut für Mineralogie, Universität Münster, Corrensstraße 24, D-48149 Münster, Germany

* : Corresponding Author

† : These authors contributed equally

Author ORCID ID:

George M. Amulele: 0000-0002-1504-4722

Anthony W. Lanati: 0000-0002-3317-5697

Simon M. Clark: 0000-0002-7488-3438

Keywords:

Electrical conductivity; Impedance Spectroscopy; Single crystal; Feldspar; Albite; High-pressure; Multi-anvil apparatus.

Abstract

Volatile-sensitive electrical soundings are becoming more widely adopted with large nationwide arrays currently being acquired globally. This boom in new data is despite a number of key uncertainties relating to the electrical responses of a wide range of minerals that make up crustal regions. Complications include the influence of mineral chemistry, hydrous or nominally hydrous phases, and oxygen fugacity on charge-carrying ion activity within a mineral substrate. Feldspars are the most abundant mineral group in the Earth's crust, comprising about 60% of its mineral assemblages and are particularly prevalent within subduction zones and lower crustal sequences. These areas are known locations where ore systems are commonly rooted making them among the most widely studied regions in Earth. To date, few studies exist that cover the electrical behavior of the intermediate feldspar mineral albite. In order to help address some of these issues and complications we have undertaken electrical conductivity investigations on a single crystal of gem-quality albite from Nuevo Casas Grande, Chihuahua, Mexico. Electrical conductivity measurements using impedance spectroscopy were performed at a pressure of 1 GPa and over a temperature range of 373 – 1273 K in a multi-anvil high-pressure apparatus. Experiments were carried out using different metal electrodes; molybdenum, nickel, and rhenium to vary the oxygen fugacity during the experiments. FTIR measurements of the starting and final materials confirm that the initial samples are completely dry but absorb an average of 67 ppm H_2O by mass during the experiments from the surrounding pressure medium materials. We observe no correlation in the amount of water absorbed in the feldspar to the oxygen fugacity under water undersaturated conditions. Our investigations show that

the activation enthalpy increases from ~0.77 eV to ~1.0 eV from the nominally hydrous to the completely dry feldspar. The activation enthalpy decreases with increasing oxygen fugacity for comparable water contents. An oxygen fugacity exponent of -0.069 is calculated at the nominal water content measured in the experiment, indicating an electrical conductivity mechanism that also involves the mobility of hydrogen.

Introduction & Background

The use of magnetotelluric (MT) soundings as a mechanism for understanding the internal structure and processes within the Earth has become increasingly common since the mid-1950s. These soundings determine the resistivity of the Earth's sub-surface by utilizing the natural variations in the Earth's magnetic and electric fields. As an electrical geophysical method, MT is highly sensitive to volatile components known to enhance the electrical response of a geological system (Adetunji et al., 2015; Cherevatova et al., 2015b; Comeau et al., 2020a; Comeau et al., 2015; Selway, 2014; Selway et al., 2019; Selway et al., 2020). It is therefore an incredibly useful tool in understanding a huge range of crustal and upper mantle processes including slab dehydration melting, partial melting of the lithosphere, the migration of brines and geothermal fluids, and long term magmatic migration in volcanic systems (Aizawa et al., 2014; Aizawa et al., 2009; Aizawa et al., 2005; Comeau et al., 2020a; Comeau et al., 2015; Díaz et al., 2012; Ingham et al., 2009). Earth materials encompass a wide range of electrical responses, ~10 orders of magnitude in most cases, and up to 22 orders in extreme instances (e.g. highly conductive sulfide ore zones near ultra-resistive quartz bodies). The bulk of the Earth is characterized by responses ranging from

84 highly resistive magmatic rocks (1x10^{6} ohm) through to ultra-conductive
85 massive sulfides (1x10^{-6} ohm) (**Figure 1**). It is therefore logical that individual
86 minerals and mineral family groups generally encompass a large range of
87 electrical responses as well. This large variance in conductive responses,
88 stemming from differing conduction mechanisms, makes the understanding of
89 the measured substrate's composition an integral prerequisite to the successful
90 interpretation of MT.

91 Feldspars are the most abundant minerals in the Earth's crust, comprising
92 about 60% of its mineral assemblages. Feldspars have a general formula $Ca_xNa_{1-x}K_{1-x}Al_{1+x}Si_{3-x}O_8$, where $0 < x < 1$, in which Ca and Na form a ternary with K. This
94 ternary is defined primarily by a solid solution relationship between the albite
95 ($Na(AlSi_3O_8)$), anorthite ($Ca(Al_2Si_2O_8)$), and orthoclase ($K(AlSi_3O_8)$ (K-feldspar)),
96 end members. Andesine ($(Ca, Na)(Al, Si)_4O_8$), the focus of this study, is an
97 intermediary feldspar formed by a solid solution of Ca and Na, residing in binary
98 space between albite and anorthite. Therefore andesine, like most calcic and
99 sodic feldspars, has limited K content. An important note for the reader is that
100 although the name andesine is still used widely in literature, recent
101 developments in the nomenclature in response to the IMA-CNMNC dominant-
102 valency rule means that the feldspar used in this study is classified as an albite
103 using modern terminology (Bosi et al., 2019). Henceforth, we will refer to our
104 samples as andesine or andesine feldspar as a matter of specificity to aid the
105 reader, except for instances where we wish to refer to the composition generally
106 as "albite". In a geological context, andesine gains its importance from being the
107 most common plagioclase feldspar in basalt and gabbro, which comprise ~70%
108 of the earth's crust as the key components of oceanic lithosphere, as well as

being a significant constituent in some other crustal rocks (i.e. anorthosites and amphibolites). Given this prevalence, knowledge of the physical and chemical properties of andesine is critically important in understanding the dynamics of the Earth's crust and upper mantle, especially in the context of subduction processes such as slab dehydration and redox melting.

Electrical conductivity measurements of crustal regions are usually obtained from magnetotelluric deep-sounding surveys (Adetunji et al., 2015; Aizawa et al., 2014; Aizawa et al., 2009; Aizawa et al., 2005; Bai et al., 2010; Cherevatova et al., 2015b; Comeau et al., 2020a; Comeau et al., 2020b; Comeau et al., 2015; Díaz et al., 2012; Heinson and White, 2005; Ingham et al., 2009; Kühn et al., 2014; Selway, 2014; Selway et al., 2019; Selway et al., 2020; Unsworth, 2010; Wannamaker et al., 2009). Complementary measurements of electrical conductivity determined in the laboratory are a necessity in modeling and interpreting field information from the magnetotelluric surveys. Several studies already report on the electrical conductivity of the various compositions of feldspathic minerals as well as their assemblages (Hu et al., 2015; Hu et al., 2014; Hu et al., 2011; Hu et al., 2013; Jones et al., 2004; Wang et al., 2014a). Through these experiments, as well as modeling, it has been established that electrical conductivity in feldspars occurs by alkali ion diffusion (i.e. via the cations Na^+, K^+, and Ca^{2+}). Diffusion progresses either by an interstitial mechanism, if the size of the alkali ion present is small relative to the parent structure of the mineral, or through vacancy substitution. Modeling results by Jones et al. (2004) have determined that in the albite and K-feldspar crystal structures, the Na^+ and K^+ ions move within the (010) plane. The concentrations and relative proportions of the different cations, Na^+, K^+, and Ca^{2+}, will affect the electrical properties of

feldspar differently. Hu et al. (2013) has reported on the effect of the Na/(Na+K) ratio on the electrical conductivity and proposed a model to this effect. Still, no generalized model that can account for the effect of all cations present in a feldspathic system exists.

From electrical conductivity measurements and models of lower crustal, dry and hydrous clinopyroxene, orthopyroxene, and plagioclase, (Yang et al., 2012; Yang et al., 2011) have suggested that the high electrical conductivities observed in most regions in the lower crust can be explained without contributions from hydrous fluids, melts or graphite films. Yang (2012) has also suggested that oxygen fugacity is directly related to the feldspar water content. Within geological systems, oxygen fugacity, (f_{O_2}), is expressed as the chemical potential of the oxygen (O_2) component. Oxygen fugacity is therefore inherently linked to the ratio between the concentrations of ferrous and ferric iron (Fe^{3+}/Fe^{2+}), as Fe is generally the most abundant redox-variable element in most magmas (i.e. FeO and Fe_2O_3) (Anenburg and O'Neill, 2019; Foley, 2011; Frost, 1991; Frost and McCammon, 2008). However, experimental systems such as single crystal measurements like those undertaken in this study are devoid of iron; therefore, the use of calibrated solid-state buffers is required. The range of buffers discussed in literature is immense and thus impossible to summarize within this contribution. Instead, we focus on undertaking our measurements at a range of f_{O_2} conditions expected to exist at varying points in the Earth. Specifically, we look to emulate aspects of the study of (Yang, 2012) in the choice of including a reduced, intermediary, and oxidized external buffer. (Yang, 2012) undertook experiments utilizing the reduced iron-wüstite (hereafter referred to as IW), intermediate nickel-nickel oxide (Ni-NiO, hereafter NNO), and oxidized

159 hematite-magnetite (hereafter MH) buffers. In this contribution we have chosen
160 to utilize solid-state metal buffers of similar f_{O_2}, namely the reduced
161 molybdenum-molybdenum oxide (Mo-MoO_2, MMO), the intermediate f_{O_2} NNO,
162 and the oxidized rhenium-rhenium oxide (Re-ReO_2, RRO) buffer. Each of these
163 buffers, whilst not physically linked to a geological setting, are used to simulate
164 conditions theorized to represent a range of geological conditions. Importantly,
165 much of the information that informs f_{O_2} conditions within the earth comes from
166 a mix of sources including physical xenolith, peridotite massifs and magmatic
167 studies (primarily via basalts), as well as theoretical, and experimental
168 laboratory studies (Foley, 2011; Frost and McCammon, 2008). Thus the buffers
169 chosen in this study were selected to encompass a range of settings from heavily
170 reduced, emulating deep mantle and deep subduction values (MMO and IW
171 (Yang, 2012) buffers), through the average oxidation state of the lithosphere and
172 subduction zones (between FMQ and NNO), and heavily oxidized reproducing
173 crustal processes such as some hydrothermal fluids and ore bodies (RRO and MH
174 (Yang, 2012)). Importantly, the coupling of the water content to the f_{O_2}
175 conditions has significant implications for processes such as dehydration and
176 redox melting within subducting slabs, as well as at the base of continental crusts
177 where granites and other silicic melts are likely to intrude. It is therefore
178 important to investigate the effect of oxygen fugacity on the electrical
179 conductivity in feldspars to provide further insight into the processes occurring
180 during subduction.

181 Given that electrical conductivity in feldspars is primarily by diffusion of
182 alkali ions, the addition of water in the structure is expected to enhance the
183 electrical conductivity (Hu et al., 2011; Maury, 1968; Wang et al., 2014a; Yang et

al., 2012),. Water can be incorporated in the feldspar structure as a hydroxyl ion or water molecule (Wright et al., 1996). Wang et al. (2014a) reports on the electrical conductivity in feldspar on hydrated samples and proposes a model that suggests a direct contribution of water to the electrical conductivity. Measurements by Ni et al. (2011) on dry and hydrous glasses, also suggest that water enhances electrical conductivity in glasses of feldspathic composition. It should be noted, however, that given the amorphous nature of glasses, conduction in these systems is not analogous to that of crystalline substrates. In addition, (Behrens, 2021) showed that hydrous species in feldspar exist predominantly as OH groups and as small amounts of molecular H_2O. The water content is determined not only by the presence of water molecules, that may be accommodated at defects sites such as at alkali vacancy sites, but also by the water pressure, i.e. the water fugacity. Coupled substitution can occur where hydrogen and alkali ions are substituted for a silicon ion with the protons residing at interstitial sites. Oxygen fugacity can, in addition, control the OH^- ion content, thereby having a strong influence on its electrical conductivity.

Therefore, while it is well established that conduction in feldspars is primarily via the diffusion of alkali ions, and that water is likely to enhance conduction it is less clear what, if any, interplay between these two systems exists. Specifically in instances where hydration is well below the saturation point of feldspars, clarification is needed on which system, the ionic (i.e. alkali diffusion), or proton (i.e. H^+ diffusion), is dominant or if some combination of both is present. In this paper, we aim to investigate the effect of nominal hydration on the electrical conductivity in Andesine feldspar under a range of oxygen fugacity conditions that are analogous to those within subduction zones

209 and crustal regimes. In order to determine the electrical conductivity response,
210 we undertake a series of complex impedance measurements at 1 GPa (~30 km
211 under continents or ~7 km under oceans) and temperatures to a maximum of
212 1273 K.
213
214 **Experimental Details**
215 All samples used in the experiments were cored from a single gem-quality
216 andesine crystal obtained from Nuevo Casas Grande in Chihuahua (Mexico). The
217 initial crystal was chemically homogenous ($Ab_{49}An_{48}Or_3$) (Table 1) and optically
218 clear with no visible fractures or alteration products. Though crystallographic
219 orientation measurements were not carried out on the crystal, coring was done
220 in the same direction for all the samples used so that the same crystal orientation
221 would be used in all experiments. The samples measured about 2.0mm in
222 diameter and 1.2mm in length. The schematic of the cell assembly used in the
223 electrical conductivity experiments is shown in **Figure 2** and is similar to that
224 used in (Amulele et al., 2019). The sample was fitted into an alumina sleeve and
225 was sealed between two metal electrodes at both ends. Metal electrodes have
226 been used as solid oxygen buffers in laboratory electrical conductivity
227 experiments at high pressures and temperatures, where evidence from scanning
228 electron microscopy of the coexistence of the metal and its metal oxide confirms
229 buffering (Dai and Karato, 2014; Dai et al., 2009). Molybdenum, nickel, and
230 rhenium metal electrodes were used in separate experiments. Metal oxide
231 buffers were selected to encompass a range of f_{O_2} conditions. Specifically, Ni-NiO
232 encompassing -23 to -9 $\log f_{O_2}$ (~ +1 to +0.73 ΔFMQ), Mo-MoO_2 -30 to -13
233 $\log f_{O_2}$ (~ -6.5 to -3.5 ΔFMQ), and Re-ReO_2 -20 to -7 $\log f_{O_2}$ (~ +3.8 to +2.5 ΔFMQ)

from 773 – 1373 K. The electrodes were stored in an oven at 393 K for at least a week before experiments and only those with a visible oxide coating were selected for use in experiments. Two Pt/Pt-10%Rh (S-type) thermocouples were connected at both ends to the electrodes. These served to measure temperature as well as complete the electrical conductivity path through the sample. Heating was achieved using a graphite furnace. The error in temperature is taken to be approximately 50°C, and is based on the design and size of the pressure cell (Leinenweber et al., 2012). 18 mm truncated edge length (TEL) MgO-Cr_2O_3 doped octahedra were used and were compressed within a cavity formed by eight, 11 mm TEL tungsten carbide anvils using a calibrated 500-ton multi-anvil high-pressure system. Effective pressure errors on experiments presented here are in the order of approximately ±0.5 GPa as expected for a multi-anvil apparatus not associated with a light source at working pressures of less than 10 GPa (Ito, 2007; and references therein; Dai and Karato, 2009; Frost et al., 2004). Before each conductivity experiment, the completed assembly was stored for at least 12 hours in oven at a temperature of 393 K to minimize the absorption of moisture from the assembly parts and ceramic cement to fill the gaps.

Impedance spectroscopy measurements were carried out, over a frequency range of 10 Hz – 1 MHz, at 1 GPa, and over a temperature range of 373 to 1273 K using a 1260 Solatron Impedance Gain-Phase Analyzer. The sample's impedance at each temperature was determined from the complex plane ($Z' - Z''$) impedance plots. The electrical conductivity was calculated at each temperature using the simple relation:

$$\sigma = \frac{L}{Z' \cdot S} \quad (1)$$

where L is the length and S the cross-sectional area of the sample, both measured by a calibrated high-resolution Leica M205C optical microscope after sample polishing at the end of each experiment. Z' is the real part of the impedance, corresponding to the intersection of the electrical response with the real axis. Samples were polished on both sides down to thicknesses of less than 2 mm (Table 1) and unpolarized FTIR measurements carried out in transmission mode to quantify the water contents. A ThermoFisher iN10 FTIR spectrometer was used for this analysis. Spectra were collected over a frequency range of 3000-4000 cm^{-1} with a 4 cm^{-1} resolution and averaged over 128 scans. EPMA measurements were carried out using a Cameca SX100 probe on the run products to determine the elemental compositions. FTIR and EPMA measurements were also collected on the parent sample.

Results

Figure 3 shows an optical image of MQ026 and SEM images of MQ046, MQ049 and MQ50, that have been sectioned and polished after the experiments. Apart from the decompression cracks observed, the samples are optically clear and chemically homogenous single crystals. Table 1 shows results of experiments carried out, including results from EPMA and FTIR analysis both before and after the electrical conductivity measurements. The electrodes used to control oxygen fugacity during runs are also listed for each experiment. Although we did not analyze the metal oxide films at the electrodes after the experiments while carrying out SEM EDS analysis, based on comparison with previous investigations of the chemical environment, pressure, temperatures (e.g. (Dai et al., 2016; Dai and Karato, 2014)) as well as from studied oxidation

kinetics of nickel (Rosa, 1982; Unutulmazsoy et al., 2017) we are confident that the systems were buffered at the respective oxygen fugacities. Oxygen fugacity values for each metal-metal oxide buffer at ambient pressure (1 bar) are calculated from expressions obtained by (O'Neill, 1986; O'Neill and Pownceby, 1993; Pownceby and O'Neill, 1994):

Mo-MoO_2: (O'Neill, 1986)

$$-603{,}268 + 337.460\,T - 20.6892\,T\,\ln T \quad (2)$$

Ni-NiO: (O'Neill and Pownceby, 1993)

$$-478{,}967 + 248.514\,T - 9.7961\,T\,\ln T \quad (3)$$

Re-ReO_2: (Pownceby and O'Neill, 1994)

$$-451{,}020 + 297.595\,T - 14.6585\,T\,\ln T \quad (4)$$

The chemical formula of the Andesine is determined to be $Ca_{0.5}Na_{0.5}Al_{1.5}Si_{2.5}O_8$. Na^+ ions are the primary contributor to electrical conductivity (Hu et al., 2011; Maury, 1968; Wang et al., 2014a; Yang et al., 2012). The concentration from K^+ ions is very low and does not significantly contribute to the electrical conductivity. The contribution from Ca^{2+} ions to electrical conductivity, on the other hand, has not been well documented yet but probably plays a greater role at temperatures above 1500K when desorption of Na has been known to take place (Campone et al., 1995). Elemental compositions taken after all the experiments are essentially the same as those in the parent crystal (Table 1). No loss of sodium or calcium to the alumina capsule is observed to take place from the samples, within the temperature range studied.

The parent crystal used as the starting sample for all electrical conductivity measurements was analyzed prior to the experiments and displayed no discernable FTIR spectra, thus indicating it to be dry. FTIR spectra

from all the samples recovered from the electrical conductivity runs (**Figure 4**) show one broad peak centered around 3400 cm^{-1} indicating that water was absorbed by the sample from the surrounding pressure medium materials at high temperature during the experiment. The 3400 cm^{-1} peak is similar to that observed in most feldspars (Behrens, 2021; Johnson and Rossman, 2003; Yang, 2012) and indicates multiple OH sites in the crystal structure (Yang et al., 2015). Molecular water also shows a broad peak about this frequency in some minerals (Kronenberg, 1994) but given that several temperature sweeps were carried out and the systems equilibrated, the water in the samples is believed not to be molecular but structural. The water contents of the recovered samples were calculated by applying Beer-Lambert's law using the expression:

$$C_w = \int_{3000}^{3700} \frac{H(\upsilon)}{I \cdot t \cdot \gamma} d\upsilon \quad (5)$$

where $\int H(\upsilon)\, d\upsilon$ is the absorption per cm integrated over the frequency range 3000 – 3700 cm^{-1}, I is the specific absorption coefficient of andesine from (Johnson and Rossman, 2003) (107,000 l mol^{-1} cm^{-2}), t is the thickness of the sample and γ is the orientation factor (1.0). The recovered MQ026 sample contains the highest content of water while MQ046 contains the least (Table 1).

Figure 5 shows the raw impedance spectra plotted in the complex plane at selected temperatures from experiment MQ046 which was buffered to RRO (other experiments spectra shown in Supplementary Figure 1). The spectra are fitted with an impedance-constant phase element (CPE) model which is able to cater for any distortions in the half circle. However, in cases where we do not obtain a good fit the intercept of the model with the Z' axis is used to determine

the resistance (Karato and Wang, 2013). Electrical conductivity is related to the activation enthalpy through the Arrhenius equation:

$$\sigma = A\ exp\left(-\frac{\Delta H}{RT}\right) \quad (6)$$

were σ is the electrical conductivity, A is the pre-exponent factor, ΔH the activation enthalpy, R the ideal gas constant, and T the temperature.

Two experiments, MQ046 and MQ049 were carried out using Re electrodes. FTIR measurements after the experiments show a nominal uptake of water in the sample from the assembly parts. Activation enthalpies of 1.0 eV and 0.77 eV and were calculated from MQ046 and MQ049, respectively. Experiment MQ050 was carried out using Mo electrodes and 51 ppm wt. H_2O was measured in the sample recovered from the experiment. An activation enthalpy of 0.81 eV was calculated from this experiment. In experiments MQ026 and MQ061, electrical conductivity measurements were carried out using Ni electrodes. In both experiments, an activation enthalpy of 0.78 eV was calculated. The same activation enthalpy is obtained despite the large variance in water contents measured in the recovered samples: 557 and 77 ppm wt. H_2O, respectively. **Figure 6** summarizes the Arrhenius relationships from all the experiments and also compares them with selected literature data (Hu et al., 2011; Maury, 1968; Wang et al., 2014a; Yang et al., 2012). **Figure 7** shows the relationship between the activation enthalpies and the water contents, with exception to the result from experiment MQ026. We observe that the activation enthalpy increases with the decrease in water content and approaches 1.0 eV for dry Andesine.

Discussion

This is the peer-reviewed, final accepted version for American Mineralogist, published by the Mineralogical Society of America.
The published version is subject to change. Cite as Authors (Year) Title. American Mineralogist, in press.
DOI: https://doi.org/10.2138/am-2021-7836. http://www.minsocam.org/

In our investigations, FTIR measurements before and after the experiments show nominal uptake of water by the samples. Yang et al. (2012) also reported a lower activation enthalpy and higher conductivity with increasing water content in plagioclase. Electrical conductivity can be expressed as a function of water content and oxygen fugacity through the more general Arrhenius equation:

$$\sigma = A \cdot C_w^r \cdot f_{O_2}^q \cdot exp\left(-\frac{\Delta H}{RT}\right) \quad (7)$$

where, C_w is the water content, f_{O_2} is the oxygen fugacity and r and q are the water content and oxygen fugacity exponents, respectively. To estimate r we carried out regression analysis, simultaneously, on the parameters A, r and ΔH using Equation (7) (taking $f_{O_2}^q$ as 1), and the measured water contents, C_w . The calculation of q is addressed in the context of the literature data below. In the nominally hydrated feldspar systems that we measured, we obtained values of r ranging between 0.52 and 0.81(Table 1).

Figure 8 shows the water content measured in the feldspar plotted as a function of oxygen fugacity, calculated at 1073 K. Our results are plotted over those from Yang (2012), which were determined under saturated hydrous conditions for each buffer. This demonstrates that our conductivity experiments were carried out in nominally hydrous systems well below the saturation limit for each buffer. Hence our experiments show a minimal effect on the water content in andesine as a function of oxygen fugacity.

Figure 9 shows the relationship of the activation enthalpies obtained as a function of oxygen fugacity determined from experiments MQ049, MQ050, and MQ061. The choice of plotting only these three experiments is based on the

379 reason that the water contents measured in the three samples are comparable,
380 within experimental error, whereas an order of magnitude increase in water
381 content is observed in MQ026, while MQ046 remains essentially dry after the
382 experiment. Based on the saturation point determined by Yang (2012) for the
383 NNO buffer, experiment MQ026 represents a case where the sample was
384 oversaturated. The fugacity values from each metal-metal oxide are obtained
385 from expressions obtained by (O'Neill, 1986; O'Neill and Pownceby, 1993;
386 Pownceby and O'Neill, 1994), and are calculated at 1 GPa. Our results show a
387 decrease in the activation enthalpy with an increase in oxygen fugacity (from
388 Mo-MoO_2 to Ni-NiO to Re-ReO_2 buffers).

389 Experiments MQ049, MQ050, and MQ061 were also used to determine
390 the value of the oxygen fugacity exponent, q, given in the electrical conductivity
391 model (**Figure 10**). The electrical conductivity in andesine decreases with an
392 increase in oxygen fugacity. An average oxygen fugacity exponent value of -0.069
393 ± 0.005 is calculated over the temperature range of 873 K – 1073 K. This value is
394 obtained by averaging the slopes of each temperature profile in Figure 10 and is
395 similar to that obtained by (Dai and Karato, 2014) for hydrous olivine in the
396 upper mantle (q = -0.066). Additionally, our q value is close to that for hydrous
397 wadsleyite (-0.058) in the mantle transition zone (Dai and Karato, 2009).
398 According to Dai and Karato (2014), a value of q = -0.069 is consistent with a
399 conductivity mechanism that involves protons. Therefore, noting that the
400 mobility of alkali ions is the dominant mechanism for electrical conductivity in
401 feldspars (i.e. ionic conduction), at least two conduction mechanisms must be
402 present, with the additional contribution being that of protons.

Defect chemistry of hydrous olivine and hydrous wadsleyite systems shows that the concentration of defects is related to the chemical environment, and can be expressed as (Dai and Karato, 2014):

$$[X] \propto f_{H_2O}^{p} \cdot f_{O_2}^{q} \cdot a_{MeO}^{s} \quad (8)$$

where p, q, and s are constants dependent on defect type, f_{H_2O} is the water fugacity and a the activity of the metal oxide buffer. In a hydrous system where electrical conductivity is mainly attributed to interstitial mobility protons (H^+), $q \approx -1/8$ and $r \approx 3/4$ in Equation (7). In the same way, within a hydrous system where electrical conductivity is attributed to alkali ions, especially when the role of water and alkali ions are interconnected through another defect site like the AlO_4^- site, such as the one presented here, the absolute value of q in both Equations (7) and (8) works out to be much lower.

Hu et al. (2013) suggests that Ca increases the Na-Na ionic distance thus increasing the hopping energy and in retrospect the activation enthalpy. Jones et al. (2004), on the other hand, calculated a lower activation enthalpy for Na^+ in K-feldspar than for K^+ in K-feldspar, concluding that a more open structure facilitates a lower energy migration pathway. This is further supported by a recent study by Hergemoller et al. (2017) who demonstrated that self-diffusion of Na^+ is ~1000 times faster than K^+ in alkali feldspar even when the concentration of Na^+ is only ~1/6 that of K^+. Diffusion of alkali ions, and therefore electrical conductivity in an alkali dominated mineral, is heavily dependent on the concentration of ions within the lattice as explained by Hergemoller et al. (2017). A finding which lends further credence to the assertion that Na^+ ions are the primary conduction mechanism in our system in part due to the low concentration of K^+ ions (Na_2O: $K_2O \approx 11:1$) within the lattice

for this sample and the larger ionic radii of K^+ (K^+= 152 pm > Na^+= 102 pm ≈ Ca^{2+}=100 pm (Shannon, 1976)). Importantly, we do not consider Ca^{2+} in our model despite it being the dominant alkali ion (26.2 wt. %) as this is a twofold problem. Firstly, there are limited contributions that discuss Ca^{2+} as a charge carrier except for those that focus on clinopyroxene group minerals. Secondly, in our system and based on the results of (Campone et al., 1995), despite the similar ionic radii of Ca^{2+} to Na^+ the temperatures under which our experiments were carried out will limit the activity of Ca^{2+} until Na^+ desorption occurs at ~1500 K. Therefore, we consider that at crustal pressures and temperatures the conductivity of feldspar group minerals will be primarily controlled by the mobility of Na^+ ions. Comparing experiment MQ050 with that of Wang et al. (2014a), where the same pre-exponent factor is obtained in both, within experimental error, there is an increase in activation enthalpy from 0.81 eV to 1.06 eV for a decrease in Ca concentration from 10.2 wt % to 0.2 wt. %, indicating that a more open structure enhances electrical conductivity. Note that there is a near factor of 2 drop in water content from Wang et al. (2014a) to MQ050.

The implication for the Earth's crust

Redox regimes within the Earth range from ~FMQ -5 at the base of the upper mantle through to ~FMQ +4 in some heavily oxidized mineral systems (Foley, 2011; Frost, 1991; Frost and McCammon, 2008). Most oceanic and subduction zone settings, however, encompass a much narrower range from ~FMQ -2 through ~FMQ+1, making the NNO buffer the most appropriate for these settings. This is with the exception of deep subduction regions where the

range of f_{O_2} values widen once more, suggesting that the MMO and IW buffers become more appropriate. MH and RRO buffers are extremely oxidizing and can be considered useful in understanding fluid processes within the crust, specifically hydrothermal and magmatic systems such as those that produce ore deposits (Richards, 2011; Richards, 2014; Richards, 2015; Wang et al., 2014b).

Albite is the most abundant feldspar within crustal regions due, in part, to its significant distribution within the oceanic lithosphere (i.e. as a major constituent in basalts and gabbros). The albite electrical conductivity model presented in this study may be useful in several ways. Specifically, in the monitoring of volcanic systems (Aizawa et al., 2014; Aizawa et al., 2009; Aizawa et al., 2005; Comeau et al., 2015; Díaz et al., 2012; Ingham et al., 2009); in understanding shallow structures such as crustal-scale brittle and ductile fracture zones (Comeau et al., 2020b; Karas et al., 2017; Ozaydin et al., 2018; Tank et al., 2018); in understanding deep earth structure and plumbing systems (Bai et al., 2010; Comeau et al., 2020a; Kühn et al., 2014; Unsworth, 2010; Wannamaker et al., 2009); in searching for resource zones (Cherevatova et al., 2015a; Corseri et al., 2017; Heinson et al., 2006); as well as in (volatile sensitive) deep earth sounding studies (Adetunji et al., 2015; Cherevatova et al., 2015a; Selway, 2014). When coupled with the distribution of other feldspar minerals our conductivity data can elucidate the mechanism of conduction across a wide range of compositions and geological settings. An area of special interest would be the lower crust, which is known to be primarily composed of clinopyroxene, orthopyroxene, and plagioclase group minerals such as andesine (albite). Electrical conductivity results obtained from magnetotelluric field measurements of the lower crust fall within the range 10^{-4} – 10^{-1} S/m (**Figure 1**).

These are much higher values than laboratory measurements that have been obtained for typical crustal minerals and mineral aggregates such as quartz, amphibole, and micas (see (Amulele et al., 2019; Hu et al., 2018)). The most likely mineral to influence the electrical conductivity of the lower crust is clinopyroxene given its high conductivity relative to other phases (i.e. olivine and andesine), and its high volume fraction (~60%) increasing the likelihood of forming interconnected networks (Yang et al., 2011). Additionally, clinopyroxene is also able to accommodate a much higher hydrogen content than other crustal minerals such as quartz, although much less than minerals with hydroxyl groups in their structure such as micas and amphiboles. Laboratory measurements indicate that for clinopyroxene to have high electrical conductivity values, it only needs to contain a few tens to a few hundred ppm wt. H_2O at lower crustal temperatures (Yang et al., 2011). Conversely, our measurements indicate that the electrical conductivity of a naturally dry plagioclase feldspar can be low and only increases above 10^{-4} S/m when it is hydrated with as little as 50 ppm wt. H_2O. These values imply a highly dry crust in certain regions of the Earth that may be dominated by plagioclase feldspars with regions of nominal hydration. Nevertheless, the contributions from the constituent minerals (clinopyroxene, orthopyroxene, and andesine) as well as contributions from partial melts and graphite films must be taken into account. Each of these components has been considered extensively when modeling conductivities in the Earth's crust and mantle, although most works focus on identifying individual contributors and no complete model for the lithosphere currently exists (Ingham et al., 2009; Jones, 1992; Özaydın and Selway, 2020).

In summary, we have presented new data on the electrical conductivity and the likely conduction mechanisms in a single crystal of andesine at crustal pressures and temperatures. Our data highlights that at 1 GPa and temperatures ranging from 573 K to 1273 K the electrical conductivity of andesine feldspar increases with increasing water content from 10^{-4} to 10^{-1} S/m. The activation enthalpy decreases with increasing water content from ~1.0 eV for the completely dry feldspar to ~0.77 eV for samples with >50 ppm H_2O. Activation enthalpy is also found to decrease mildly with increasing oxygen fugacity for comparable water contents. Given this moderate decrease it can be said that conductivity, expressed as $\log_{10} A$, increases with increasing oxidation (i.e. ReO < NNO < MMO). Finally, we report an oxygen fugacity exponent of -0.069 within the nominally hydrated experiments which, based on literature, indicates an electrical conductivity mechanism that involves the mobility of hydrogen as well as alkali ions. Our results are, therefore, of specific use in the modeling and interpretation of MT responses recorded within the initial stages of subduction down to depths of ~30 km into the lithosphere, where a slab would be hydrated, and within redox regime of the NNO buffer.

Acknowledgment

The authors thank L. Spruženiece for the supply of the Nuevo Casas Grande andesine used at the starting material in this study as well as many helpful discussions about felspars. We would like to thank Prof. G. Heinson, University of Adelaide, for the loan of the 1260 Solatron Impedance Gain-Phase Analyzer. The authors acknowledge useful discussions around oxygen fugacity from M. Anenburg; comments and helpful insights from M Klöcking; and the

generation of conductivity models to provide some of the values in Figure 1 by S. Özaydin using the MATE software.

An earlier version of this manuscript was improved by the insights of two anonymous reviewers and editor from a previous submission to another journal, for which we thank them immensely. We gratefully acknowledge and thank our reviewers, including Dr. Xiaozhi Yang for their constructive comments and insights from the two American Mineralogist submissions. We thank Dr. Daniel Hummer for extensive editorial assistance and useful comments on the manuscript during the original submission, and during resubmission. We also acknowledge and thank Dr. Zhicheng Jing for editorial handling of the resubmission.

Author Contributions:

GMA designed the study with useful discussions from SMC. GMA and AWL carried out the experiments. GMA undertook analysis and interpretation of results in collaboration with AWL. GMA wrote the initial manuscript. AWL undertook extensive edits, submitted, and revised the paper with GMA. All authors have contributed to, read, and agreed to the final manuscript.

Funding:

This is contribution xxx from the ARC Centre of Excellence for Core to Crust Fluid Systems (http://www.ccfs.mq.edu.au). The analytical data were obtained using instrumentation funded by DEST Systemic Infrastructure Grants, ARC LIEF, NCRIS/AuScope, industry partners, and Macquarie University. High-pressure equipment and consumables were obtained from an ARC LIEF (LE160100103) to

552 Prof. S. F. Foley (SMC CI), and an ARC Discovery (DP160103502) to SMC.
553 Additional laboratory and consumables funding were provided through the ARC
554 Centre of Excellence for Core to Crust Fluid Systems. Some of the FTIR analysis
555 was obtained using the Bruker FTIR V70 FTIR system located at the University of
556 Hawaii, instrument funded by NSF grant No. EAR-0957137. AWL was supported
557 during his Masters of Research by and Macquarie University Faculty of Science
558 HDR funds. AWL is currently funded by a Deutscher Akademischer
559 Austauschdienst (German Research Exchange Service) Research Grant (Grant
560 No. 57507869) and an Australian Government Research Training Program (RTP)
561 Stipend and RTP Fee-Offset Scholarship through Macquarie University
562 (Allocation No. 2018177).

References

Adetunji, A.Q., Ferguson, I.J., and Jones, A.G. (2015) Imaging the mantle lithosphere of the Precambrian Grenville Province: large-scale electrical resistivity structures. Geophysical Journal International, 201(2), 1040-1061.

Aizawa, K., Koyama, T., Hase, H., Uyeshima, M., Kanda, W., Utsugi, M., Yoshimura, R., Yamaya, Y., Hashimoto, T., Yamazaki, K.i., Komatsu, S., Watanabe, A., Miyakawa, K., and Ogawa, Y. (2014) Three-dimensional resistivity structure and magma plumbing system of the Kirishima Volcanoes as inferred from broadband magnetotelluric data. Journal of Geophysical Research: Solid Earth, 119(1), 198-215.

Aizawa, K., Ogawa, Y., and Ishido, T. (2009) Groundwater flow and hydrothermal systems within volcanic edifices: Delineation by electric self-potential and magnetotellurics. Journal of Geophysical Research: Solid Earth, 114(B1), n/a-n/a.

Aizawa, K., Yoshimura, R., Oshiman, N., Yamazaki, K., Uto, T., Ogawa, Y., Tank, S.B., Kanda, W., Sakanaka, S., Furukawa, Y., Hashimoto, T., Uyeshima, M., Ogawa, T., Shiozaki, I., and Hurst, A.W. (2005) Hydrothermal system beneath Mt. Fuji volcano inferred from magnetotellurics and electric self-potential. Earth and Planetary Science Letters, 235(1–2), 343-355.

Amulele, G.M., Lanati, A.W., and Clark, S.M. (2019) Electrical conductivity studies on silica phases and the effects of phase transformation. American Mineralogist, 104(12), 1800-1805.

586 Anenburg, M., and O'Neill, H.C. (2019) Redox in Magmas: Comment on a Recent
587 Treatment of the Kaiserstuhl Volcanics (Braunger et al., Journal of
588 Petrology, 59, 1731–1762, 2018) and Some Other Misconceptions. Journal
589 of Petrology, 60(9), 1825–1832.

590 Bai, D., Unsworth, M.J., Meju, M.A., Ma, X., Teng, J., Kong, X., Sun, Y., Sun, J., Wang,
591 L., Jiang, C., Zhao, C., Xiao, P., and Liu, M. (2010) Crustal deformation of the
592 eastern Tibetan plateau revealed by magnetotelluric imaging. Nature
593 Geosci, 3(5), 358-362.

594 Behrens, H. (2021) Hydrogen defects in feldspars: defect properties and
595 implications for water solubility in feldspar. Physics and Chemistry of
596 Minerals, 48.

597 Bosi, F., Hatert, F., Halenius, U., Pasero, M., Ritsuro, M., and Mills, S.J. (2019) On
598 the application of the IMA-CNMNC dominant-valency rule to complex
599 mineral compositions. Mineralogical Magazine, 83(5), 627-632.

600 Campone, P., Magliocco, M., Spinolo, G., and Vedda, A. (1995) Ionic transport in
601 crystalline SiO2: The role of alkali-metal ions and hydrogen impurities.
602 Physical Review B, 52(22), 15903-15908.

603 Cherevatova, M., Smirnov, M.Y., Jones, A.G., Pedersen, L.B., Becken, M., Biolik, M.,
604 Cherevatova, M., Ebbing, J., Gradmann, S., Gurk, M., Hübert, J., Jones, A.G.,
605 Junge, A., Kamm, J., Korja, T., Lahti, I., Löwer, A., Nittinger, C., Pedersen,
606 L.B., Savvaidis, A., and Smirnov, M. (2015a) Magnetotelluric array data
607 analysis from north-west Fennoscandia. Tectonophysics, 653, 1-19.

608 Cherevatova, M., Smirnov, M.Y., Jones, A.G., Pedersen, L.B., Becken, M., Biolik, M.,
609 Cherevatova, M., Ebbing, J., Gradmann, S., Gurk, M., Hubert, J., Jones, A.G.,
610 Junge, A., Kamm, J., Korja, T., Lahti, I., Lower, A., Nittinger, C., Pedersen,
611 L.B., Savvaidis, A., Smirnov, M., and Grp, M.W. (2015b) Magnetotelluric
612 array data analysis from north-west Fennoscandia. Tectonophysics, 653,
613 1-19.

614 Comeau, M.J. (2015) Electrical Resistivity Structure of the Altiplano-Puna Magma
615 Body and Volcan Uturuncu from Magnetotelluric Data, Doctor of
616 Philosophy. University of Alberta.

617 Comeau, M.J., Becken, M., Connolly, J.A.D., Grayver, A.V., and Kuvshinov, A.V.
618 (2020a) Compaction-Driven Fluid Localization as an Explanation for
619 Lower Crustal Electrical Conductors in an Intracontinental Setting.
620 Geophysical Research Letters, 47(19).

621 Comeau, M.J., Becken, M., Kaufl, J.S., Grayver, A.V., Kuvshinov, A.V., Tserendug, S.,
622 Batmagnai, E., and Demberel, S. (2020b) Evidence for terrane boundaries
623 and suture zones across Southern Mongolia detected with a 2-
624 dimensional magnetotelluric transect. Earth Planets and Space, 72(1).

625 Comeau, M.J., Unsworth, M.J., Ticona, F., and Sunagua, M. (2015) Magnetotelluric
626 images of magma distribution beneath Volcan Uturuncu, Bolivia:
627 Implications for magma dynamics. Geology, 43(3), 243-246.

628 Corseri, R., Senger, K., Selway, K., Abdelmalak, M.M., Planke, S., and Jerram, D.A.
629 (2017) Magnetotelluric evidence for massive sulphide mineralization in

intruded sediments of the outer Voring Basin, mid-Norway. Tectonophysics, 706, 196-205.

Dai, L., and Karato, S.I. (2009) Electrical conductivity of wadsleyite at high temperatures and high pressures. Earth and Planetary Science Letters, 287(1-2), 277-283.

Dai, L.D., Hu, H.Y., Li, H.P., Wu, L., Hui, K.S., Jiang, J.J., and Sun, W.Q. (2016) Influence of temperature, pressure, and oxygen fugacity on the electrical conductivity of dry eclogite, and geophysical implications. Geochemistry Geophysics Geosystems, 17(6), 2394-2407.

Dai, L.D., and Karato, S. (2014) Influence of oxygen fugacity on the electrical conductivity of hydrous olivine: Implications for the mechanism of conduction. Physics of the Earth and Planetary Interiors, 232, 57-60.

Dai, L.D., Li, H.P., Hu, H.Y., and Shan, S.M. (2009) Novel technique to control oxygen fugacity during high-pressure measurements of grain boundary conductivities of rocks. Review of Scientific Instruments, 80(3).

Díaz, D., Brasse, H., and Ticona, F. (2012) Conductivity distribution beneath Lascar volcano (Northern Chile) and the Puna, inferred from magnetotelluric data. Journal of Volcanology and Geothermal Research, 217–218, 21-29.

Duba, A., Heard, H.C., and Schock, R.N. (1974) Electrical-Conductivity of Olivine at High-Pressure and under Controlled Oxygen Fugacity. Journal of Geophysical Research, 79(11), 1667-1673.

652 Duba, A.G., and Shankland, T.J. (1982) Free Carbon and Electrical-Conductivity in
653 the Earths Mantle. Geophysical Research Letters, 9(11), 1271-1274.

654 Fitzpatrick, A.D. (2006) Scale dependent electrical properties of sulphide
655 deposits. University of Tasmania.

656 Foley, S.F. (2011) A Reappraisal of Redox Melting in the Earth's Mantle as a
657 Function of Tectonic Setting and Time. Journal of Petrology, 52(7-8),
658 1363-1391.

659 Frost, B.R. (1991) Introduction to oxygen fugacity and its petrologic importance.
660 Reviews in Mineralogy and Geochemistry, 25(1), 1-9.

661 Frost, D.J., and McCammon, C.A. (2008) The redox state of Earth's mantle. Annual
662 Review of Earth and Planetary Sciences, 36, 389-420.

663 Haak, V., and Hutton, R. (1986) Electrical resistivity in continental lower crust. In
664 J.B. Dawson, D.A. Carswell, J. Hall, and K.H. Wedepohl, Eds. The Nature of
665 the Lower Continental Crust, 24. Geological Society Special Publication.

666 Heinson, G., and White, A. (2005) Electrical resistivity of the Northern Australian
667 lithosphere: Crustal anisotropy or mantle heterogeneity? Earth and
668 Planetary Science Letters, 232(1-2), 157-170.

669 Heinson, G.S., Direen, N.G., and Gill, R.M. (2006) Magnetotelluric evidence for a
670 deep-crustal mineralizing system beneath the Olympic Dam iron oxide
671 copper-gold deposit, southern Australia. Geology, 34(7), 573-576.

672 Heinson, G.S., and Lilley, F.E.M. (1993) An Application of Thin-Sheet
673 Electromagnetic Modeling to the Tasman Sea. Physics of the Earth and
674 Planetary Interiors, 81(1-4), 231-251.

675 Hergemoller, F., Wegner, M., Deicher, M., Wolf, H., Brenner, F., Hutter, H., Abart,
676 R., and Stolwijk, N.A. (2017) Potassium self-diffusion in a K-rich single-
677 crystal alkali feldspar. Physics and Chemistry of Minerals, 44(5), 345-351.

678 Hirsch, L.M., Shankland, T.J., and Duba, A.G. (1993) Electrical-Conduction and
679 Polaron Mobility in Fe-Bearing Olivine. Geophysical Journal International,
680 114(1), 36-44.

681 Hu, H.Y., Dai, L.D., Li, H.P., Hui, K.S., and Li, J. (2015) Temperature and pressure
682 dependence of electrical conductivity in synthetic anorthite. Solid State
683 Ionics, 276, 136-141.

684 Hu, H.Y., Dai, L.D., Li, H.P., Jiang, J.J., and Hui, K.S. (2014) Electrical conductivity of
685 K-feldspar at high temperature and high pressure. Mineralogy and
686 Petrology, 108(5), 609-618.

687 Hu, H.Y., Dai, L.D., Li, H.P., Sun, W.Q., and Li, B.S. (2018) Effect of dehydrogenation
688 on the electrical conductivity of Fe-bearing amphibole: Implications for
689 high conductivity anomalies in subduction zones and continental crust.
690 Earth and Planetary Science Letters, 498, 27-37.

691 Hu, H.Y., Li, H.P., Dai, L.D., Shan, S.M., and Zhu, C.M. (2011) Electrical conductivity
692 of albite at high temperatures and high pressures. American Mineralogist,
693 96(11-12), 1821-1827.

-. (2013) Electrical conductivity of alkali feldspar solid solutions at high temperatures and high pressures. Physics and Chemistry of Minerals, 40(1), 51-62.

Ingham, M.R., Bibby, H.M., Heise, W., Jones, K.A., Cairns, P., Dravitzki, S., Bennie, S.L., Caldwell, T.G., and Ogawa, Y. (2009) A magnetotelluric study of Mount Ruapehu volcano, New Zealand. Geophysical Journal International, 179(2), 887-904.

Johnson, E.A., and Rossman, G.R. (2003) The concentration and speciation of hydrogen in feldspars using FTIR and H-1 MAS NMR spectroscopy. American Mineralogist, 88(5-6), 901-911.

Jones, A. (1992) Electrical conductivity of the continental lower crust. In D.M. Fountain, R.J. Arculus, and R.W. Kay, Eds. Continental Lower Crust, p. 81. Elsevier.

Jones, A., Islam, M.S., Mortimer, M., and Palmer, D. (2004) Alkali ion migration in albite and K-feldspar. Physics and Chemistry of Minerals, 31(5), 313-320.

Karas, M., Tank, S.B., and Ozaydin, S. (2017) Electrical conductivity of a locked fault: investigation of the Ganos segment of the North Anatolian Fault using three-dimensional magnetotellurics. Earth Planets and Space, 69.

Karato, S., and Wang, D.J. (2013) Electrical Conductivity of Minerals and Rocks. In S. Karato, Ed. Physics and Chemistry of the Deep Earth. John Wiley & Sons, Ltd.

715 Kariya, K.A., and Shankland, T.J. (1983) Electrical-Conductivity of Dry Lower
716 Crustal Rocks. Geophysics, 48(1), 52-61.

717 Keller, G. (1966) Electrical Properties of Rocks and Minerals. Handbook of
718 Physical Constants, 97. The Geological Society of America.

719 Kronenberg, A.K. (1994) Hydrogen Speciation and Chemical Weakening of
720 Quartz. Silica: Physical Behavior, Geochemistry and Materials
721 Applications, 29, 123-176.

722 Kühn, C., Küster, J., and Brasse, H. (2014) Three-dimensional inversion of
723 magnetotelluric data from the Central Andean continental margin. Earth,
724 Planets and Space, 66(1), 112.

725 Leinenweber, K.D., Tyburczy, J.A., Sharp, T.G., Soignard, E., Diedrich, T., Petuskey,
726 W.B., Wang, Y.B., and Mosenfelder, J.L. (2012) Cell assemblies for
727 reproducible multi-anvil experiments (the COMPRES assemblies).
728 American Mineralogist, 97(2-3), 353-368.

729 Lizarralde, D., Chave, A., Hirth, G., and Schultz, A. (1995) Northeastern Pacific
730 Mantle Conductivity Profile from Long-Period Magnetotelluric Sounding
731 Using Hawaii-to-California Submarine Cable Data. Journal of Geophysical
732 Research-Solid Earth, 100(B9), 17837-17854.

733 Maury, R. (1968) Conductivilite electrique des tectosilicates. II. Discussion des
734 resultats. Bulletin de la Societe Francaise de Mineralogie et
735 Cristallographie, 91, 355 - 366.

736 Nesbitt, B.E. (1993) Electrical Resistivities of Crustal Fluids. Journal of
737 Geophysical Research-Solid Earth, 98(B3), 4301-4310.

738 Ni, H.W., Keppler, H., Manthilake, M.A.G.M., and Katsura, T. (2011) Electrical
739 conductivity of dry and hydrous NaAlSi3O8 glasses and liquids at high
740 pressures. Contributions to Mineralogy and Petrology, 162(3), 501-513.

741 O'Neill, H.S.C. (1986) Mo-Mo02 (MOM) oxygen buffer and the free energy of
742 formation of Mo02. American Mineralogist, 71, 1007 - 1010.

743 O'Neill, H.S.C., and Pownceby, M.I. (1993) Thermodynamic data from redox
744 reactions at high temperatures. I. An experimental and theoretical
745 assessment of the electrochemical method using stabilized zirconia
746 electrolytes, with revised values for the Fe - "FeO", Co- CoO, Ni - NiO and
747 Cu- CuzO oxygen buffers, and new data for the W-WO2 buffer.
748 Contributions to Mineralogy and Petrology, 114, 296 - 314.

749 Özaydın, S., and Selway, K. (2020) MATE: An analysis tool for the interpretation
750 of magnetotelluric models of the mantle. Geochemistry Geophysics
751 Geosystems, 21.

752 Ozaydin, S., Tank, S.B., and Karas, M. (2018) Electrical resistivity structure at the
753 North-Central Turkey inferred from three-dimensional magnetotellurics.
754 Earth Planets and Space, 70.

755 Palacky, G.J. (1987) 3. Resistivity Characteristics of Geologic Targets.
756 Electromagnetic Methods in Applied Geophysics: Volume 1, Theory, p. 52-
757 129.

758 Pownceby, M.I., and O'Neill, H.S.C. (1994) Thermodynamic data from redox
759 reactions at high temperatures. IV. Calibration of the Re-ReO2 oxygen
760 buffer from EMF and NiO + Ni-Pd redox sensor measurements.
761 Contributions to Mineralogy and Petrology, 118, 130 - 137.

762 Presnall, D.C., Simmons, C.L., and Porath, H. (1972) Changes in Electrical
763 Conductivity of a Synthetic Basalt during Melting. Journal of Geophysical
764 Research, 77(29), 5665-&.

765 Richards, J.P. (2011) Magmatic to hydrothermal metal fluxes in convergent and
766 collided margins. Ore Geology Reviews, 40(1), 1-26.

767 -. (2014) Discussion of Sun et al. (2013): The link between reduced porphyry
768 copper deposits and oxidized magmas. Geochimica Et Cosmochimica Acta,
769 126, 643-645.

770 -. (2015) The oxidation state, and sulfur and Cu contents of arc magmas:
771 implications for metallogeny. Lithos, 233, 27-45.

772 Rosa, C.J. (1982) The High-Temperature Oxidation of Nickel. Corrosion Science,
773 22(12), 1081-1088.

774 Schultz, A., Kurtz, R.D., Chave, A.D., and Jones, A.G. (1993) Conductivity
775 Discontinuities in the Upper-Mantle beneath a Stable Craton. Geophysical
776 Research Letters, 20(24), 2941-2944.

777 Selway, K. (2014) On the Causes of Electrical Conductivity Anomalies in
778 Tectonically Stable Lithosphere. Surveys in Geophysics, 35(1), 219-257.

779 Selway, K., O'Donnell, J.P., and Ozaydin, S. (2019) Upper Mantle Melt Distribution
780 From Petrologically Constrained Magnetotellurics. Geochemistry
781 Geophysics Geosystems, 20(7), 3328-3346.

782 Selway, K., Smirnov, M.Y., Beka, T., O'Donnell, J.P., Minakov, A., Senger, K., Faleide,
783 J.I., and Kalscheuer, T. (2020) Magnetotelluric Constraints on the
784 Temperature, Composition, Partial Melt Content, and Viscosity of the
785 Upper Mantle Beneath Svalbard. Geochemistry Geophysics Geosystems,
786 21(5).

787 Shannon, R.D. (1976) Revised Effective Ionic-Radii and Systematic Studies of
788 Interatomic Distances in Halides and Chalcogenides. Acta
789 Crystallographica Section A, 32(Sep1), 751-767.

790 Simpson, F. (2002) A comparison of electromagnetic distortion and resolution of
791 upper mantle conductivities beneath continental Europe and the
792 Mediterranean using islands as windows. Physics of the Earth and
793 Planetary Interiors, 129(1-2), 117-130.

794 Simpson, F., and Bahr, K. (2005) Practical Magnetotellurics. Cambridge
795 University Press.

796 Tank, S.B., Ozaydin, S., and Karas, M. (2018) Revealing the electrical properties of
797 a gneiss dome using three-dimensional magnetotellurics: Burial and
798 exhumation cycles associated with faulting in Central Anatolia, Turkey.
799 Physics of the Earth and Planetary Interiors, 283, 26-37.

800 Telford, W.M., Geldart, L.P., and Sheriff, R.E. (1990) Magnetic Methods. Applied
801 Geophysics, p. 62-135. Cambridge University Press.

802 Tyburczy, J.A., and Waff, H.S. (1983) Electrical-Conductivity of Molten Basalt and
803 Andesite to 25 Kilobars Pressure - Geophysical Significance and
804 Implications for Charge Transport and Melt Structure. Journal of
805 Geophysical Research, 88(Nb3), 2413-2430.

806 Unsworth, M. (2010) Magnetotelluric Studies of Active Continent–Continent
807 Collisions. Surveys in Geophysics, 31(2), 137-161.

808 Unutulmazsoy, Y., Merkle, R., Fischer, D., Mannhart, J., and Maier, J. (2017) The
809 oxidation kinetics of thin nickel films between 250 and 500 degrees C.
810 Physical Chemistry Chemical Physics, 19(13), 9045-9052.

811 Utada, H., Koyama, T., Shimizu, H., and Chave, A.D. (2003) A semi-global
812 reference model for electrical conductivity in the mid-mantle beneath the
813 north Pacific region. Geophysical Research Letters, 30(4).

814 Waff, H.S. (1974) Theoretical Considerations of Electrical-Conductivity in a
815 Partially Molten Mantle and Implications for Geothermometry. Journal of
816 Geophysical Research, 79(26), 4003-4010.

817 Wang, D.J., and Karato, S.I. (2013) Electrical conductivity of talc aggregates at 0.5
818 GPa: influence of dehydration. Physics and Chemistry of Minerals, 40(1),
819 11-17.

Wang, D.J., Yu, Y.J., and Zhou, Y.S. (2014a) Electrical conductivity anisotropy in alkali feldspar at high temperature and pressure. High Pressure Research, 34(3), 297-308.

Wang, R., Richards, J.P., Hou, Z.Q., Yang, Z.M., Gu, Z.B., and DuFrane, S.A. (2014b) Increasing Magmatic Oxidation State from Paleocene to Miocene in the Eastern Gangdese Belt, Tibet: Implication for Collision-Related Porphyry Cu-Mo +/- Au Mineralization. Economic Geology, 109(7), 1943-1965.

Wannamaker, P.E., Caldwell, T.G., Jiracek, G.R., Maris, V., Hill, G.J., Ogawa, Y., Bibby, H.M., Bennie, S.L., and Heise, W. (2009) Fluid and deformation regime of an advancing subduction system at Marlborough, New Zealand. Nature, 460(7256), 733-736.

Wright, K., Freer, R., and Catlow, C.R.A. (1996) Water-related defects and oxygen diffusion in albite: A computer simulation study. Contributions to Mineralogy and Petrology, 125(2-3), 161-166.

Xu, Y.S., Poe, B.T., Shankland, T.J., and Rubie, D.C. (1998) Electrical conductivity of olivine, wadsleyite, and ringwoodite under upper-mantle conditions. Science, 280(5368), 1415-1418.

Xu, Y.S., and Shankland, T.J. (1999) Electrical conductivity of orthopyroxene and its high pressure phases. Geophysical Research Letters, 26(17), 2645-2648.

840 Yang, X.Z. (2012) An experimental study of H solubility in feldspars: Effect of
841 composition, oxygen fugacity, temperature and pressure and implications
842 for crustal processes. Geochimica Et Cosmochimica Acta, 97, 46-57.

843 Yang, X.Z., Keppler, H., McCammon, C., and Ni, H.W. (2012) Electrical conductivity
844 of orthopyroxene and plagioclase in the lower crust. Contributions to
845 Mineralogy and Petrology, 163(1), 33-48.

846 Yang, X.Z., Keppler, H., McCammon, C., Ni, H.W., Xia, Q.K., and Fan, Q.C. (2011)
847 Effect of water on the electrical conductivity of lower crustal
848 clinopyroxene. Journal of Geophysical Research-Solid Earth, 116.

849 Yang, Y., Xia, Q.K., and Zhang, P.P. (2015) Evolution of OH groups in diopside and
850 feldspars with temperature. European Journal of Mineralogy, 27(2), 185-
851 192.

852

853

Figure Captions:

Figure 1: Electrical conductivity ranges for i) Earth materials, ii) Major mantle minerals, iii) Crust and upper mantle (from MT sounding), iv) Analytical electrical response models . Fields labelled a) – e) are based on values from (Utada et al., 2003) and represent the range of electrical responses from the crust through to the deep mantle (including transition zone (TZ)) beneath the North Pacific where a) represents lithosphere (0 – 100 Km); b) the upper mantle (100 – 410 Km, olivine stable); c) upper TZ (410 – 550 km, wadsleyite stable); d) lower TZ (550 – 660 Km, ringwoodite stable); and e) lower mantle (>660 Km). An upper and lower bound for each field for i) – iv) is given by a resistivity (ohm meter) and conductivity (S/m) with the bars colored across a gradient from red (conductive) to purple (resistive) illustrating electrical response relative to other materials. Data references: graphite (Duba and Shankland, 1982; Simpson and Bahr, 2005); sulfides (Fitzpatrick, 2006; Keller, 1966; Telford et al., 1990)); brines and geothermal fluids (Nesbitt, 1993); graphitic schist (Comeau, 2015); seawater ((Simpson and Bahr, 2005) (Comeau, 2015); partial melt (as 5% basaltic melt from 1000 – 1200°C) (Presnall et al., 1972; Tyburczy and Waff, 1983; Waff, 1974); pure melt (basalt 1200°C) (Tyburczy and Waff, 1983; Waff, 1974); weathered granite, sandstone and limestone (Comeau, 2015); igneous rocks (resistive bound 500°C, conductive bound 1000°C), basalt, gabbro and granite (Kariya and Shankland, 1983); olivine, wet (Lizarralde et al., 1995), dry (Duba et al., 1974; Hirsch et al., 1993; Xu et al., 1998); pyroxene (dry) (Xu and Shankland, 1999); Mid-Lower Continental Crust (MLCC) (Haak and Hutton, 1986; Jones, 1992); Upper Continental Mantle (UCM) (Heinson and Lilley, 1993; Lizarralde et al., 1995); Upper Oceanic Mantle (UOM) (Schultz et al., 1993;

879 Simpson, 2002); Values for wet/dry pyroxenite (as Ol-websterite: ol 29%, opx
880 41%, cpx 30%, grt 0%) and peridotite (as lherzolite: ol 60%, opx 31%, cpx 9%,
881 grt 0% (0 – 100 km), and ol 60.6%, opx 28.4%, cpx 6%, grt 5% (100 – 200 km)
882 were generated using the MATE program with wet values being modeled
883 containing 100 ppm H_2O (Özaydın and Selway, 2020). After (Fitzpatrick, 2006;
884 Palacky, 1987; Simpson and Bahr, 2005) and (Comeau, 2015).
885
886 Figure 2: A schematic of the electrical conductivity high-pressure temperature
887 cell used in the multi-anvil experiments (Amulele et al., 2019)
888
889 Figure 3: Optical image of MQ026 and SEM images of MQ046, MQ049 and MQ50,
890 sectioned and polished experimental run products. The samples were optically
891 clear single gem-quality crystals of andesine.
892
893 Figure 4: FTIR Spectra of nominally hydrous andesine obtained after electrical
894 conductivity experiments at high pressure and temperature. Inset shows
895 detailed view of spectra from experiments MQ046 (brown), MQ049 (red),
896 MQ050 (blue), and MQ061 (green).
897
898 Figure 5: Selected impedance spectra collected during the second temperature
899 increase in experiment MQ046. The spectra are fitted with an impedance-
900 constant phase element model which is able to cater for any distortions in the
901 half circle. However, in cases where we do not obtain a good fit the intercept of
902 the model with the Z^'axis is used to determine the resistance (Karato and Wang,

903 2013). Impedance spectra for all experiments can be found in supplementary
904 figure 1.
905
906 Figure 6: Comparing Arrhenius plots obtained in experiments MQ026, MQ046,
907 MQ049, MQ050 and MQ061 with literature data from (Hu et al., 2011; Maury,
908 1968; Wang et al., 2014a; Yang et al., 2012)
909
910 Figure 7: Relationship between the activation enthalpy and the water content
911 from experiments MQ046, MQ049, MQ050 and MQ061, with exception of
912 experiment MQ026 which had an order of magnitude higher water content. The
913 red line shows the best fit model with the anchor point being MQ050.
914
915 Figure 8: Water content measured in andesine as a function of oxygen fugacity,
916 calculated at 1073 K. Comparison is made with the saturation curve determined
917 by Yang (2012) for each buffer (black squares), showing that experiments
918 presented here (red triangles) represent water undersaturated conductivity
919 measurements. The blue triangle shows MQ046 (2.74 ppm H_2O), and the green
920 triangle shows the excluded MQ026 experiment which, for its buffer, is heavily
921 oversaturated (NNO, 557 ppm H_2O).
922
923 Figure 9: Activation enthalpy as a function of oxygen fugacity in feldspar at 1 GPa
924
925 Figure 10: The effect of oxygen fugacity on electrical conductivity in andesine at
926 1.0 GPa, temperature range of 873–1073 K, and an average water content of ~67
927 ppm wt. H_2O for experiments MQ049, MQ050 and MQ061.

This is the peer-reviewed, final accepted version for American Mineralogist, published by the Mineralogical Society of America.
The published version is subject to change. Cite as Authors (Year) Title. American Mineralogist, in press.
DOI: https://doi.org/10.2138/am-2021-7836. http://www.minsocam.org/

928 *Table 1: A summary of experimental conditions and results from the experimental runs carried out*

Exp.	T (K)	Cycles[1]	SiO_2	Al_2O_3	Na_2O	K_2O	CaO	Water content (ppm wt. H_2O)	ΔH (eV)	$Log_{10}A$	*r*	Electrodes	Thickness (cm)
Parent			56.7	27.2	5.6	0.5	10.2	Dry					
MQ026	573 - 1273	2	56.1	27.5	5.5	0.5	10.1	557	0.78 ±0.03	1.66 ± 0.70	0.81 ± 0.02	Ni-NiO	0.13
MQ046	573 - 1273	2	56.2	27.5	5.6	0.5	10.1	2.74	1.00 ± 0.06	1.10 ± 0.96	0.00 ± 0.02	Re-ReO_2	0.17
MQ049	573 - 1273	2	56.2	27.6	5.6	0.6	10.1	72	0.77 ± 0.03	0.80 ± 0.70	0.66 ± 0.02	Re-ReO_2	0.18
MQ050	573 - 1173	2	56.2	27.6	5.7	0.5	10.1	51	0.81 ± 0.02	1.58 ± 0.69	0.77 ± 0.02	Mo-MoO_2	0.13
MQ061[2]	573 - 1273	2	N.D.	N.D.	N.D.	N.D.	N.D.	77	0.78 ± 0.07	1.05 ± 1.04	0.52 ± 0.02	Ni-NiO	0.16

Notes:

[1]: Conductivity cycles comprise both a heating and a cooling phase within which conductivity was measured at 100 K intervals.

[2]: Run product for MQ061 was lost in preparation for chemical analysis. We therefore assume the composition of MQ026 to be analogous.

N.D.: Not Determined

929

This is the peer-reviewed, final accepted version for American Mineralogist, published by the Mineralogical Society of America.
The published version is subject to change. Cite as Authors (Year) Title. American Mineralogist, in press.
DOI: https://doi.org/10.2138/am-2021-7836. http://www.minsocam.org/

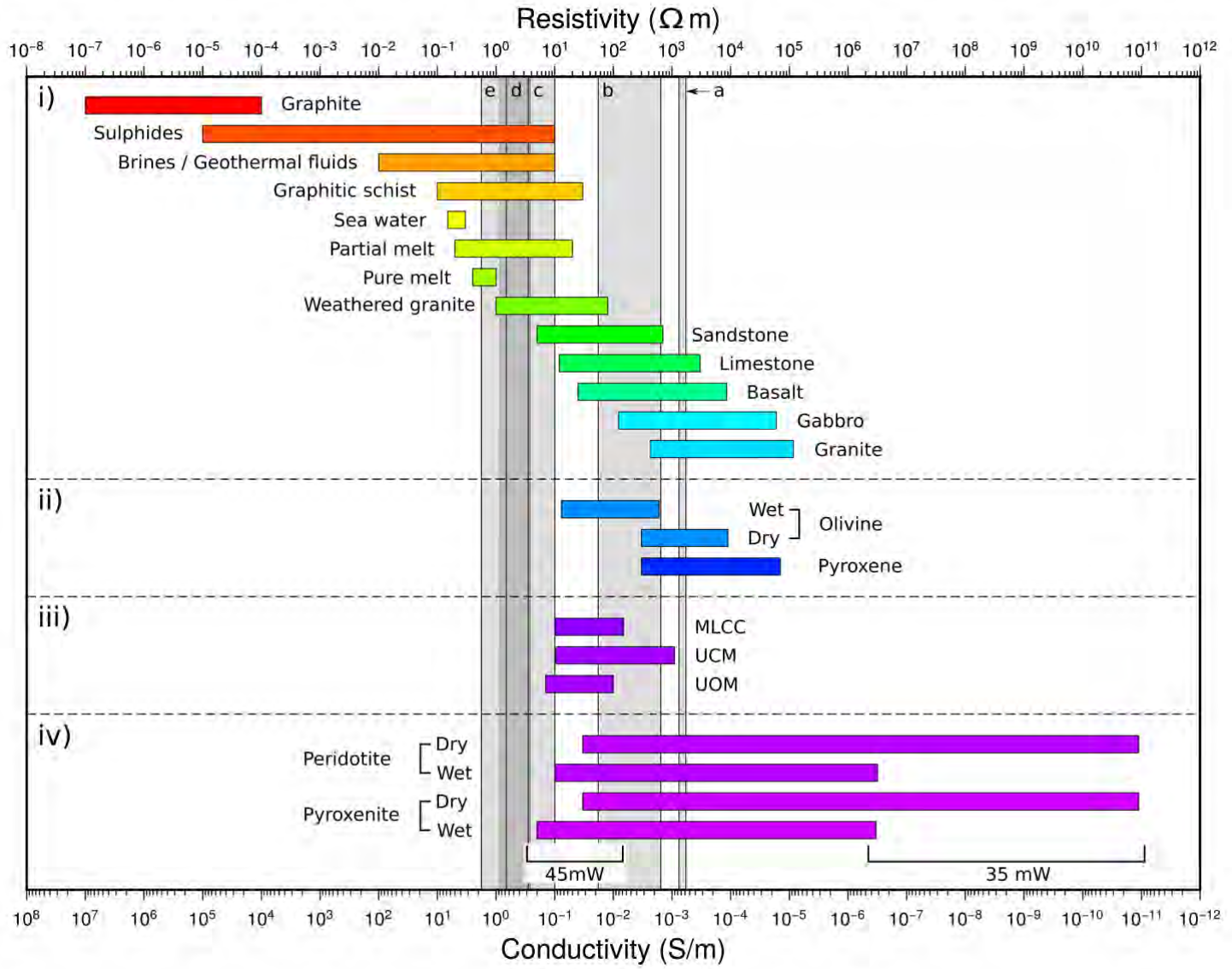

930

Figure 1: Electrical conductivity ranges for i) Earth materials, ii) Major mantle minerals, iii) Crust and upper mantle (from MT sounding), iv) Analytical electrical response models . Fields labelled a) – e) are based on values from (Utada et al., 2003) and represent the range of electrical responses from the crust through to the deep mantle (including transition zone (TZ)) beneath the North Pacific where a) represents lithosphere (0 – 100 Km); b) the upper mantle (100 – 410 Km, olivine stable); c) upper TZ (410 – 550 km, wadsleyite stable); d) lower TZ (550 – 660 Km, ringwoodite stable); and e) lower mantle (>660 Km). An upper and lower bound for each field for i) – iv) is given by a resistivity (ohm meter) and conductivity (S/m) with the bars colored across a gradient from red (conductive) to purple (resistive) illustrating electrical response relative to other materials. Data references: graphite (Duba and Shankland, 1982; Simpson and Bahr, 2005); sulfides (Fitzpatrick, 2006; Keller, 1966; Telford et al., 1990)); brines and geothermal fluids (Nesbitt, 1993); graphitic schist (Comeau, 2015); seawater ((Simpson and Bahr, 2005) (Comeau, 2015); partial melt (as 5% basaltic melt from 1000 – 1200°C) (Presnall et al., 1972; Tyburczy and Waff, 1983; Waff, 1974); pure melt (basalt 1200°C) (Tyburczy and Waff, 1983; Waff, 1974); weathered granite, sandstone and limestone (Comeau, 2015); igneous rocks (resistive bound 500°C, conductive bound 1000°C), basalt, gabbro and granite (Kariya and Shankland, 1983); olivine, wet (Lizarralde et al., 1995), dry (Duba et al., 1974; Hirsch et al., 1993; Xu et al., 1998); pyroxene (dry) (Xu and Shankland, 1999); Mid-Lower Continental Crust (MLCC) (Haak and Hutton, 1986; Jones, 1992); Upper Continental Mantle (UCM) (Heinson and Lilley, 1993; Lizarralde et al., 1995); Upper Oceanic Mantle (UOM) (Schultz et al., 1993; Simpson, 2002); Values for wet/dry pyroxenite (as Ol-websterite: ol 29%, opx 41%, cpx 30%, grt 0%) and peridotite (as lherzolite: ol 60%, opx 31%, cpx 9%, grt 0% (0 – 100 km), and ol 60.6%, opx 28.4%, cpx 6%, grt 5% (100 – 200 km) were generated using the MATE

947 program with wet values being modeled containing 100 ppm H_2O (Özaydın and Selway, 2020). After (Fitzpatrick, 2006; Palacky, 1987;

948 Simpson and Bahr, 2005) and (Comeau, 2015).

949
950

This is the peer-reviewed, final accepted version for American Mineralogist, published by the Mineralogical Society of America.
The published version is subject to change. Cite as Authors (Year) Title. American Mineralogist, in press.
DOI: https://doi.org/10.2138/am-2021-7836. http://www.minsocam.org/

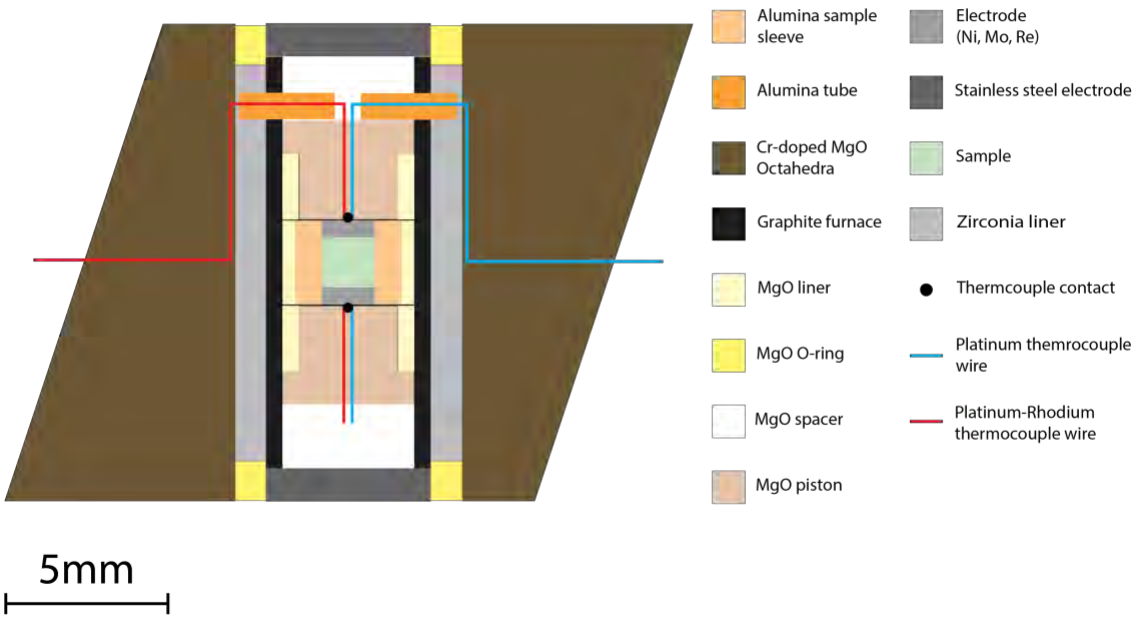

Figure 2: A schematic of the electrical conductivity high-pressure temperature cell used in the multi-anvil experiments (Amulele et al., 2019)

This is the peer-reviewed, final accepted version for American Mineralogist, published by the Mineralogical Society of America.
The published version is subject to change. Cite as Authors (Year) Title. American Mineralogist, in press.
DOI: https://doi.org/10.2138/am-2021-7836. http://www.minsocam.org/

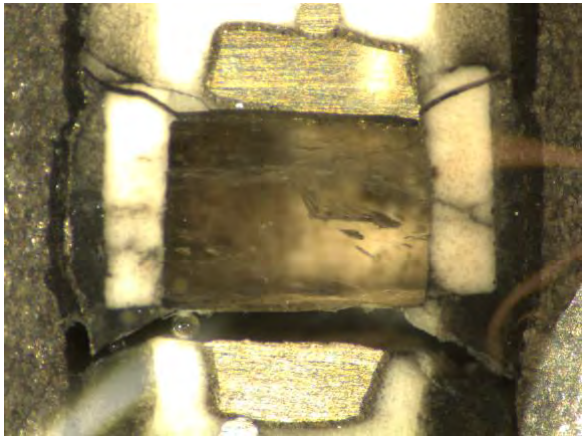

MQ026

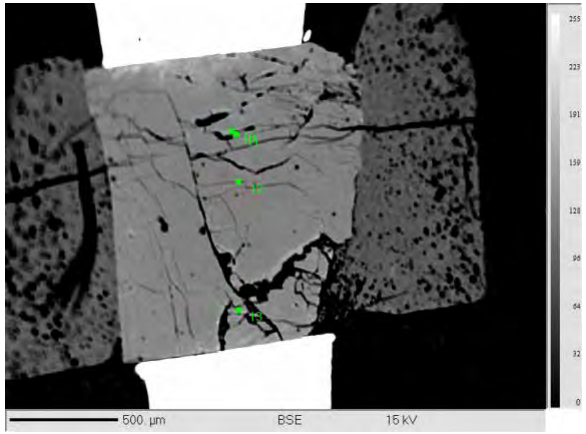

MQ046

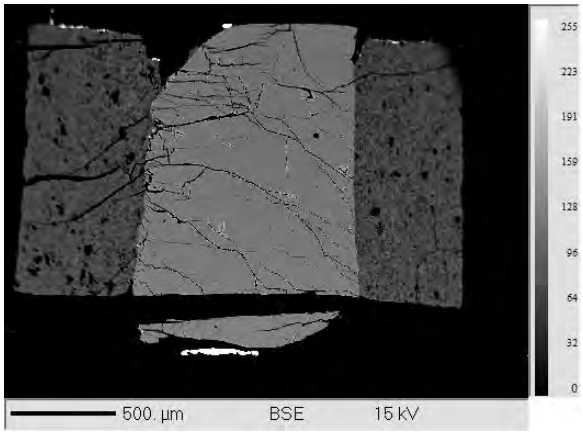

MA049

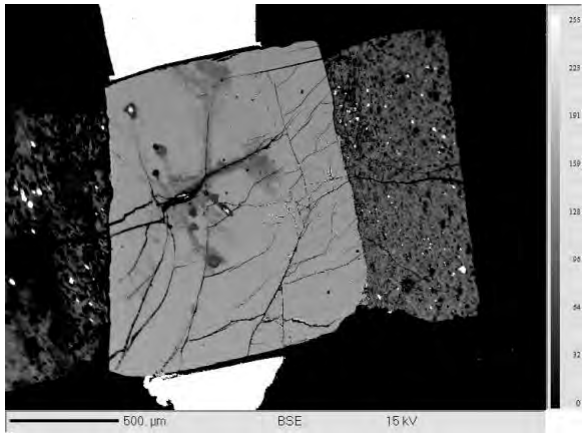

MQ050

954 Figure 3: Optical image of MQ026 and SEM images of MQ046, MQ049 and MQ50, sectioned and polished experimental run products.
955 The samples were optically clear single gem-quality crystals of andesine.
956

This is the peer-reviewed, final accepted version for American Mineralogist, published by the Mineralogical Society of America.
The published version is subject to change. Cite as Authors (Year) Title. American Mineralogist, in press.
DOI: https://doi.org/10.2138/am-2021-7836. http://www.minsocam.org/

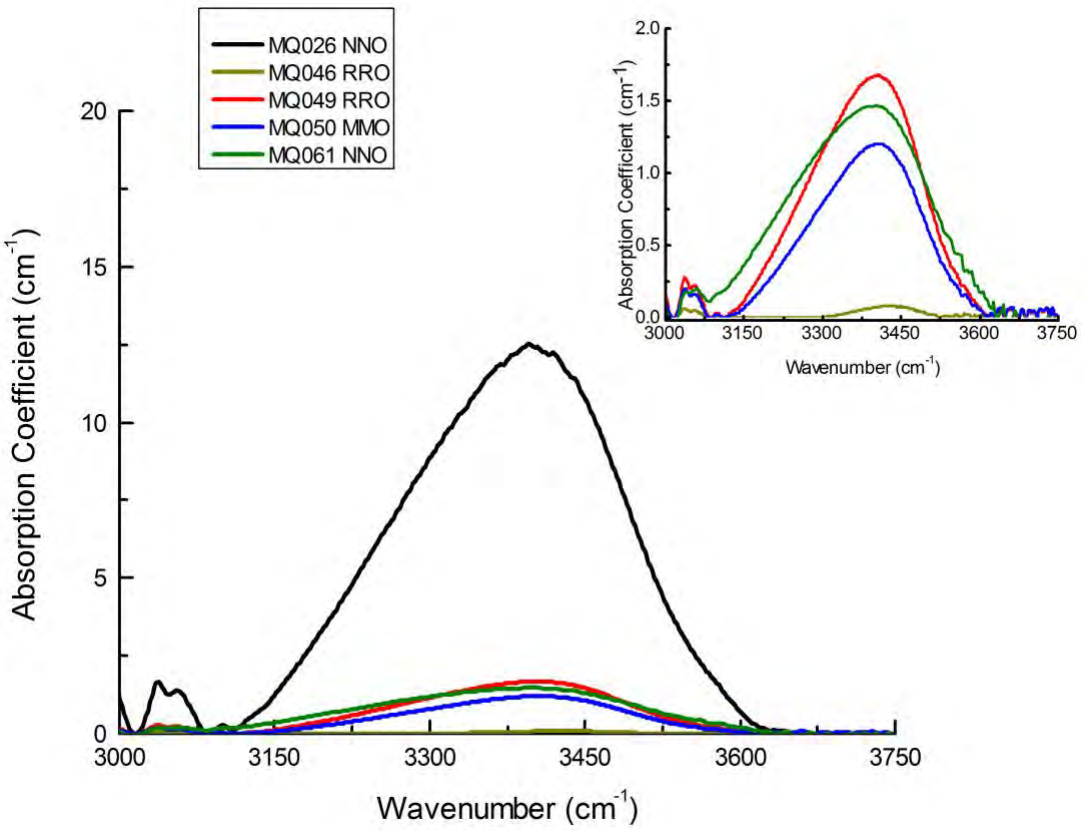

957

958 Figure 4: FTIR Spectra of nominally hydrous andesine obtained after electrical conductivity experiments at high pressure and

959 temperature. Inset shows detailed view of spectra from experiments MQ046 (brown), MQ049 (red), MQ050 (blue), and MQ061 (green).

This is the peer-reviewed, final accepted version for American Mineralogist, published by the Mineralogical Society of America.
The published version is subject to change. Cite as Authors (Year) Title. American Mineralogist, in press.
DOI: https://doi.org/10.2138/am-2021-7836. http://www.minsocam.org/

960

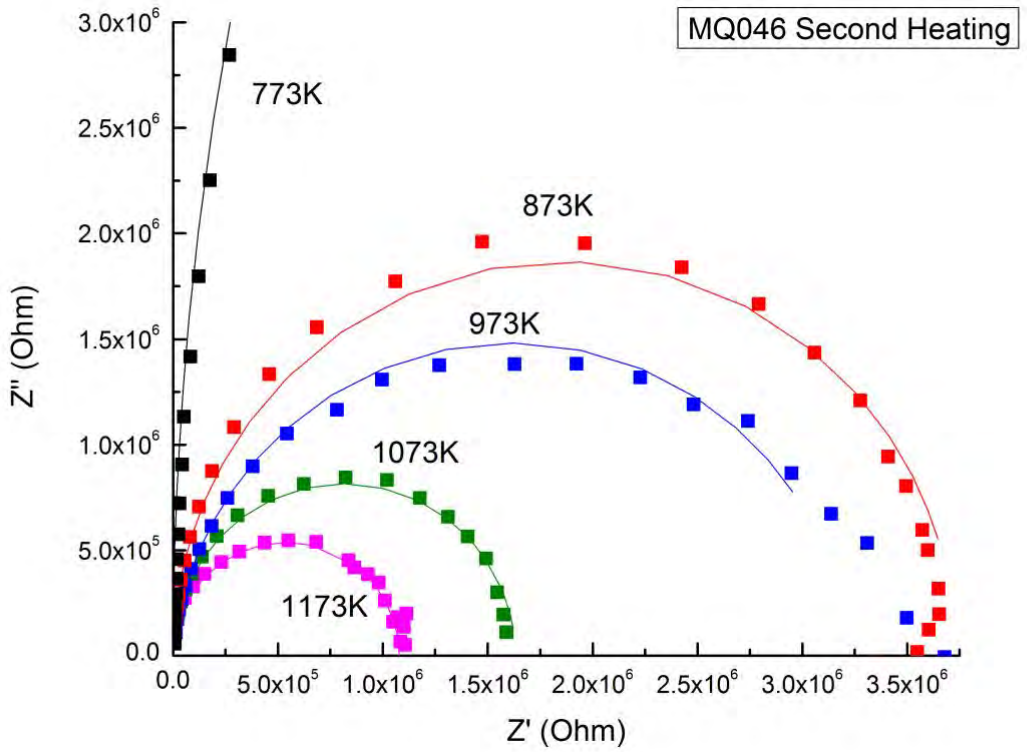

961

962 Figure 5: Selected impedance spectra collected during the second temperature increase in experiment MQ046. The spectra are fitted
963 with an impedance-constant phase element model which is able to cater for any distortions in the half circle. However, in cases where
964 we do not obtain a good fit the intercept of the model with the Z' axis is used to determine the resistance (Karato and Wang, 2013).
965 Impedance spectra for all experiments can be found in supplementary figure 1.
966

967
968

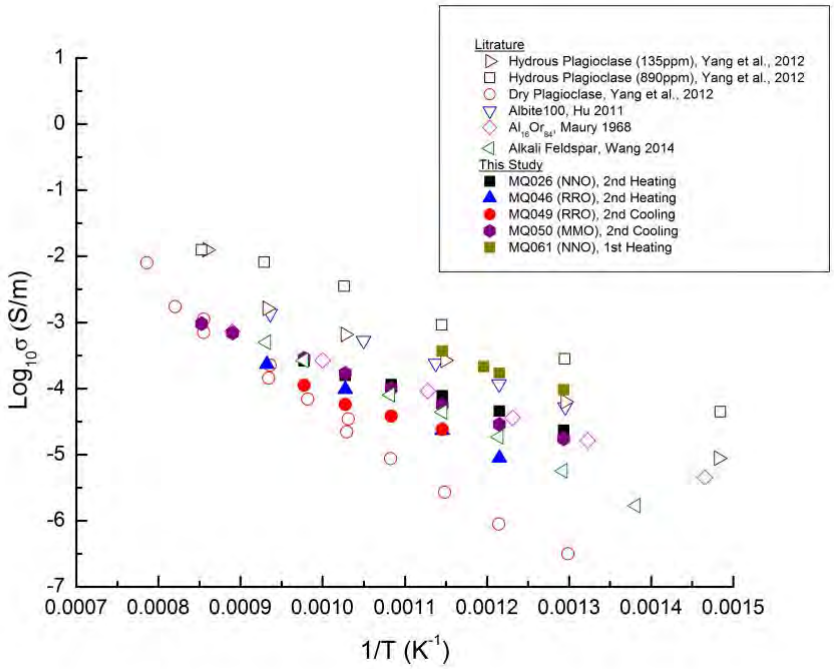

969
970 Figure 6: Comparing Arrhenius plots obtained in experiments MQ026, MQ046, MQ049, MQ050 and MQ061 with literature data from (Hu
971 et al., 2011; Maury, 1968; Wang et al., 2014a; Yang et al., 2012)

This is the peer-reviewed, final accepted version for American Mineralogist, published by the Mineralogical Society of America.
The published version is subject to change. Cite as Authors (Year) Title. American Mineralogist, in press.
DOI: https://doi.org/10.2138/am-2021-7836. http://www.minsocam.org/

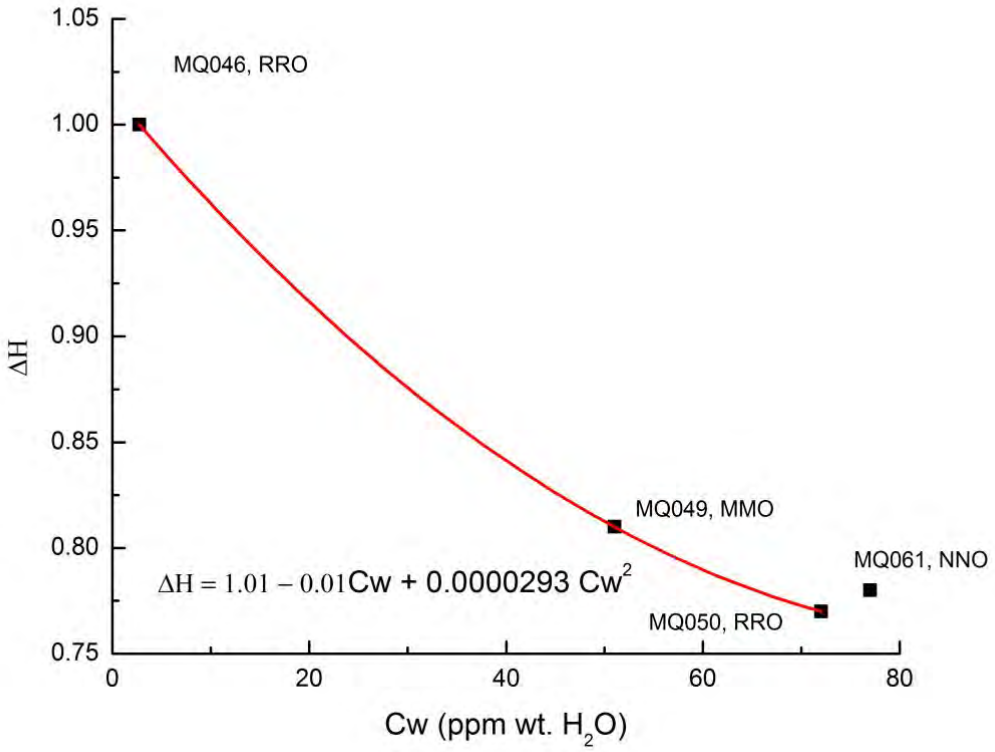

Figure 7: Relationship between the activation enthalpy and the water content from experiments MQ046, MQ049, MQ050 and MQ061, with exception of experiment MQ026 which had an order of magnitude higher water content. The red line shows the best fit model with the anchor point being MQ050.

This is the peer-reviewed, final accepted version for American Mineralogist, published by the Mineralogical Society of America.
The published version is subject to change. Cite as Authors (Year) Title. American Mineralogist, in press.
DOI: https://doi.org/10.2138/am-2021-7836. http://www.minsocam.org/

978

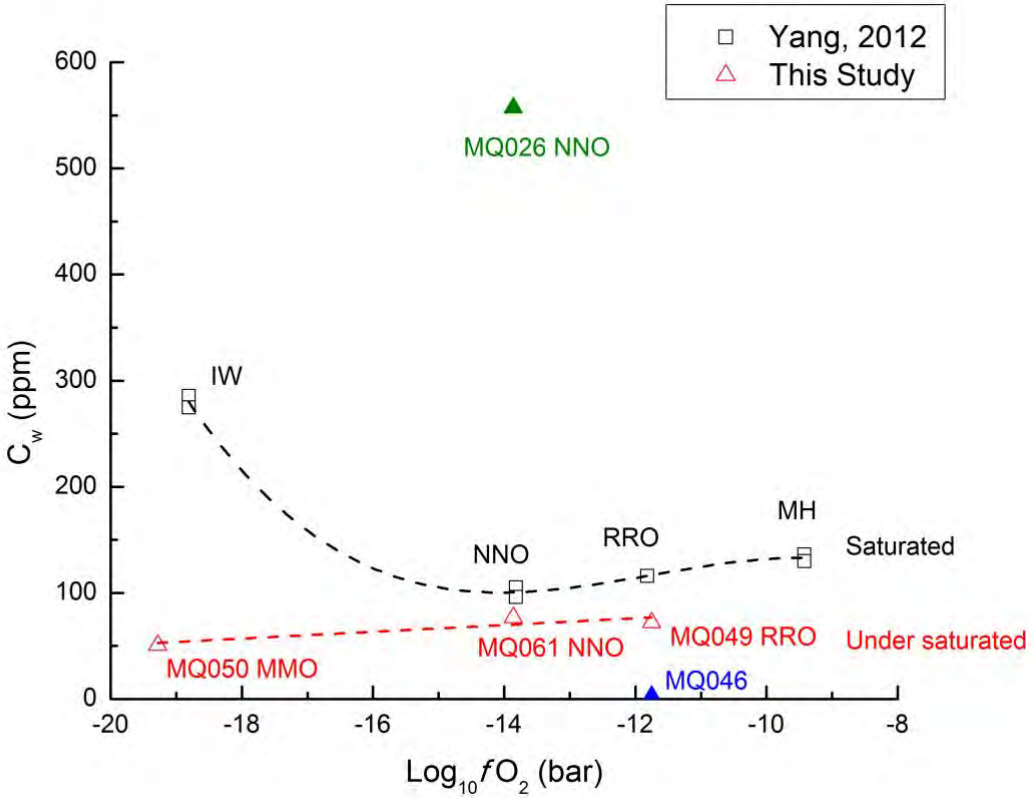

979
980 Figure 8: Water content measured in andesine as a function of oxygen fugacity, calculated at 1073 K. Comparison is made with the
981 saturation curve determined by Yang (2012) for each buffer (black squares), showing that experiments presented here (red triangles)
982 represent water undersaturated conductivity measurements. The blue triangle shows MQ046 (2.74 ppm H_2O), and the green triangle
983 shows the excluded MQ026 experiment which, for its buffer, is heavily oversaturated (NNO, 557 ppm H_2O).

This is the peer-reviewed, final accepted version for American Mineralogist, published by the Mineralogical Society of America.
The published version is subject to change. Cite as Authors (Year) Title. American Mineralogist, in press.
DOI: https://doi.org/10.2138/am-2021-7836. http://www.minsocam.org/

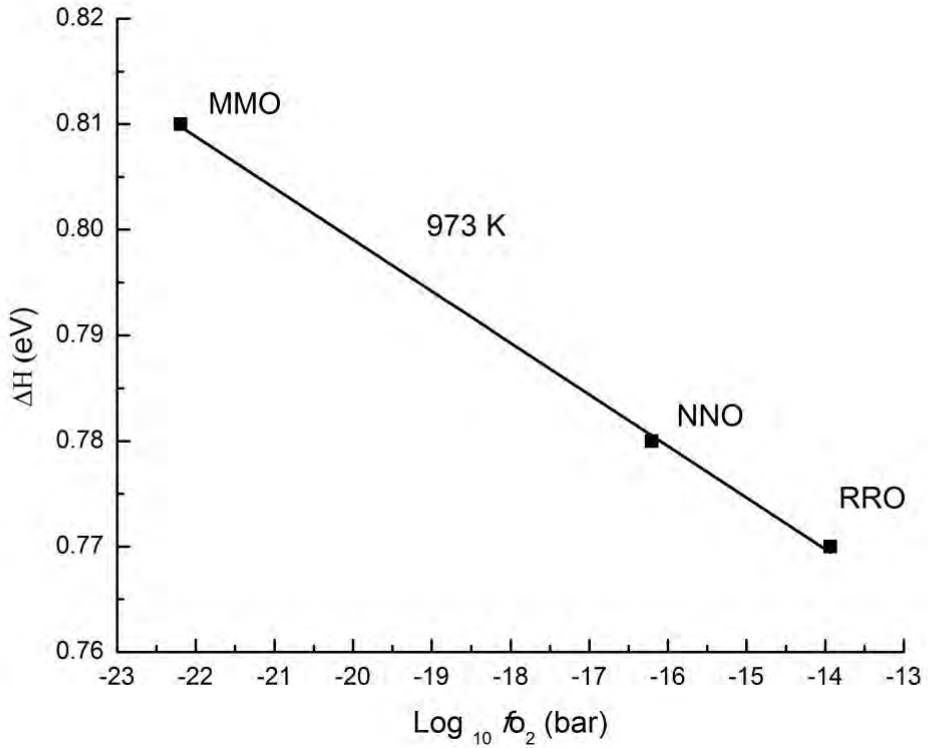

Figure 9: Activation enthalpy as a function of oxygen fugacity in andesine at 1.0 GPa

This is the peer-reviewed, final accepted version for American Mineralogist, published by the Mineralogical Society of America.
The published version is subject to change. Cite as Authors (Year) Title. American Mineralogist, in press.
DOI: https://doi.org/10.2138/am-2021-7836. http://www.minsocam.org/

986

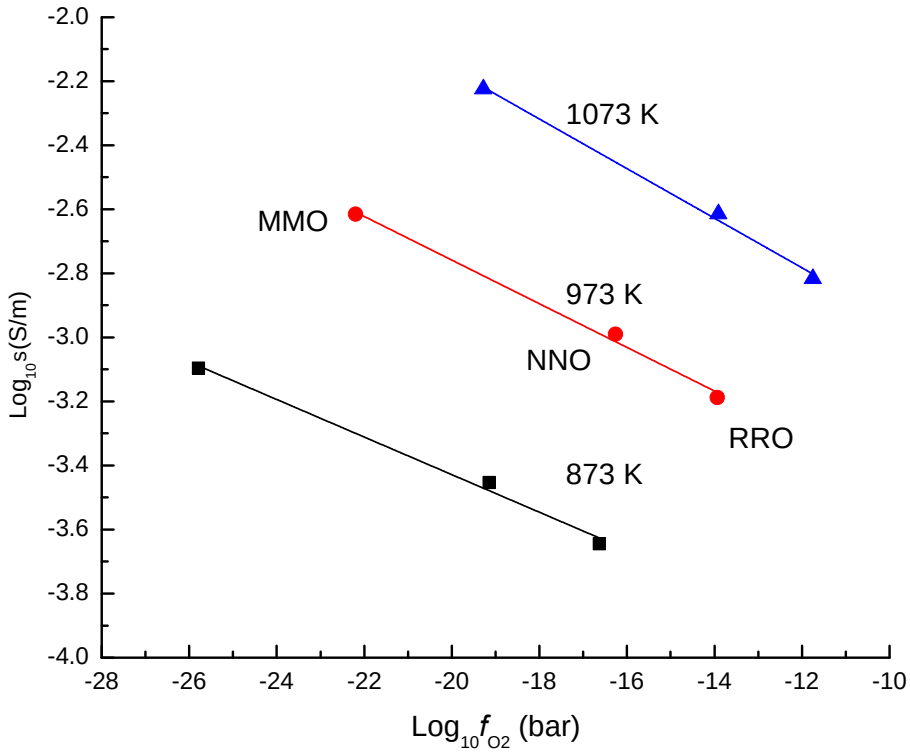

987

988 Figure 10: The effect of oxygen fugacity on electrical conductivity in andesine at 1.0 GPa, temperature range of 873–1073 K, and an

989 average water content of ~67 ppm wt. H_2O for experiments MQ049, MQ050 and MQ061.

990